
PROGRESSIVE DOMAIN ADAPTATION WITH CONTRASTIVE LEARNING FOR OBJECT DETECTION IN THE SATELLITE IMAGERY

Debojyoti Biswas
Computer Science
Texas State University
San Marcos, TX 78666
ubq3@txstate.edu

Jelena Tešić
Computer Science
Texas State University
San Marcos, TX 78666
jtesic@txstate.edu

January 18, 2023

ABSTRACT

Recent increases in computational power and the volume of the aerial imagery acquired and stored. The growing interest in automated overhead analytic (piracy, natural resource protection, agriculture) drives the research in aerial object localization and identification effectiveness to be comparable to object detection and recognition in consumer datasets. Images in aerial datasets are very large in resolution, and each frame contains many dense and small objects. State-of-the-art detection methods fail to capture small objects, local features, and region proposals for densely overlapped objects in aerial imagery due to the high variation of object sizes in satellite imagery with respect to the image size and high variation of content. Aerial imagery content varies greatly within the dataset due to the large change in lighting conditions, and the type of ground imagery captures from high altitudes. The variation is even higher between different datasets as object sizes, class distributions, image acquisition, and weather conditions can vary even more drastically. Thus, Domain Adaptation (DA) has been introduced as a band-aid to alleviate the degradation of object identification in previously unseen datasets. In this paper, we propose a small object detection pipeline that improves the feature extraction process by spatial pyramid pooling, cross-stage partial networks, heat-map-based region proposal network, and objects localization and identification through a novel image difficulty score that adapts the overall focal loss measure based on the image difficulty. Next, we propose novel contrastive learning with progressive domain adaptation to produce domain-invariant features across aerial datasets using local and global features. Effective analysis and illustration of different performance metrics and challenges show that our proposed method is comparable to the current State-of-Art models and creates a first-ever Domain Adaptation benchmark for the object detection task in highly imbalanced satellite datasets with large domain gaps and dominant small objects.

Keywords Object Detection · Small Objects · Satellite Imagery · Domain Adaptation · Aerial Imagery · Contrastive Learning

1 Introduction

The next frontier in precision agriculture, emergency rescue systems, terrestrial and naval traffic monitoring, and industrial surveillance is the integration of accurate automated object location from an overhead satellite, and aerial imagery [3, 4, 5, 6]. Aerial images are taken from high altitudes (e.g. satellite), and the number of objects per image is over 100, and the object size is often less than 0.01% of the size of an image. Examples of consumer images and overhead images of similar pixel size are illustrated in Figure 1. Continuous improvements in deep neural network (DNN) models, combined with increased access to computational resources, have improved object detection methods in consumer images [7, 8, 9]. Still, the improvements have not generalized to the overhead imagery [10, 11, 12]. State-of-the-art object detection and domain adaptation (DA) modeling approaches developed for consumer images do



Figure 1: Consumer [1] and aerial images [2] example

not translate to overhead imagery due to visual variation within the image, variation among the images in the collection, the relative object size with respect to the image, the image size, and the density and number of objects in an image as illustrated in Figure 1.

Deep neural networks require large and diverse amounts of annotated training data to guarantee reliable object localization in unseen datasets. Collecting and annotating aerial datasets has proven to be a difficult and complex task due to the high number of small and dense objects per image [13]. To date, there are only three datasets with rich class distribution being used to benchmark the results to date: DOTA2.0[14], and DIOR [2] are two satellite image collections and VisDrone is the overhead drone collection [15]. Domain adaptation is the task of successfully sharing acquired knowledge (in terms of annotations and learned models) in the source domain with the target domain. Domain adaptation has risen as one of the approaches to speed up the pseudo-labeling of objects in the target domain using source labels. Recent work on domain adaptation for object recognition in consumer image datasets successfully addresses weather, lighting conditions, geological variance, variation in image quality, and cross-camera adaptation by aligning the global feature distribution of data from the origin and target domains [16]. Large variations in overhead image datasets from the source to the target dataset render the domain adaptation task challenging. State-of-the-art work of unsupervised domain adaptation for aerial imagery uses the reconstructed feature alignment method instead of adversarial-based feature alignment to avoid background noise alignment [17]. However, recent work [17] does not address the challenges in large satellite benchmark datasets, does not address the high density of objects in an image, and does not consider a high domain gap from the geographical variance of the datasets.

Contrastive learning evaluates pair-to-pair relationships by measuring the similarities between different pairs such as query-positive or query-negative. This paper introduces the first domain adaptation benchmark for large-scale satellite image datasets. To reduce the global gap between the source and target domains, we create two intermediate domains using the CycleGAN modeling [18]. Next is the local and global feature extraction from feature pyramid network (FPN) layers using the adapted domain adaptation approach. Finally, we evaluate domain adaptation approaches and introduce the noise-contrastive estimation (InfoNCE) loss to produce domain-invariant features. The proposed pipeline efficiently automates object localization and identification in previously unseen satellite imagery, as evaluated on the DOTA2.0 dataset. Section 2 summarizes related work, and Section 4 introduces the proposed methodology for domain adaptation using contrastive learning and improvements to the object detection training pipeline. In Section 5 we present the experimental results on real satellite image sets and show that the proposed approach outperforms the state-of-the-art baseline model in detecting small and overlapped objects and producing higher mean average precision (mAP) over overlapping classes.

2 Related Work

Object Detection State-of-the-art object detectors are single-stage or multistage detectors. Single-stage detectors are object detection networks without a region proposal network (RPN) module [19, 12, 20] and are mainly based on a different scale and aspect ratios of the anchor boxes. Single-stage object detection architectures were shown to miss a significant number of small objects in satellite imagery and require a good anchor design for better performance [14, 21]. Multistage detectors are often more reliable [22, 23] due to extra effort to improve the regions of interest of the images. Multistage detectors use region proposal networks (RPN) [24, 25] to filter out positive instances from the image with the help of IOU and the non-maximum suppression technique (NMS). Heatmap-based region proposal approach with balanced positive/negative examples per batch uses a Gaussian filter, creating a heat-map peak at the object’s center to define proposal regions [26]. The anchor to the object is the region’s center based on location, not a region overlap [8]. Thus, the one anchor per object eliminates the need for the non-maximum suppression filtering of the overlapping proposals without affecting the quality of the proposal.

Small and dense Object Detection As the size of the object decreases, the chances of losing local information in deep layers increase significantly. The outcome of the small object detection depends on how well the backbone network [27, 28] captures the region features from the input image. Next, different scale features from different stages of the backbone have been successfully used for different scale predictions. The feature pyramid network (FPN) layer upscales the bottom-up features with the combination of lateral connections to create top-bottom features for scale prediction [29]. FPN also helps to strengthen low spatially rich features by combining semantically rich features by combining low-level and high-level features together with the fuse connection and upsample method. Zhu et al. [30] use two different fusion methods. This improved FPN module uses a similarity-based fusion method which is capable of extracting information for various sizes of instances. It has been shown that the proposed pixel-level appearance features do not contain enough information [31, 32] to localize small objects in an image. Context-based feature extraction techniques [32, 33, 34] are much more robust for complex object and scene detection and perform better in benchmark datasets. The latest publication by Wu et al. [32] uses a global context aggregation module and the feature refinement module to build Global Context-Weaving Network. To perform better with small objects, Gong et al. [33] propose using the context-regions-of-interests mining layer in the CNN model and using foreground proposals for extracting context features. Zhang et al. [34] use attention mechanisms for salient object detection. They propose an attention module to supervise features from different receptive fields and represent better relationships among context information for better results. The contextually based bidirectional feature fusion of neighboring pixels alleviates the issue of detecting objects with high variance in the background, and loosely packed objects [35].

Domain Adaptation for Object Detection Domain Adaptation techniques are used to handle the problem of domain change between source and target data sets. In the last couple of years, the unsupervised Generative Adversarial Network (GAN) has played a critical role in solving the domain shift problem. Multitask generative adversarial network upsamples blur small images into clear fine-scale images with the multitask GAN module and improve object detection [36]. The GAN-based approach expands object detection in consumer images to other domains [37, 38]. Adversarial learning has been applied to align the distribution of characteristics between domains and perform progressive domain adaptation to address the problem of large domain gaps [37]. Edge-enhanced superresolution GAN (EESRGAN) improves the detection of small objects using a super-resolution GAN, an edge-enhanced network, and a detection network [39].

On the other hand, maximum mean discrepancy and central moment discrepancy approaches are also successful in producing domain-invariant features through the alignment of feature space. Long et al. proposed DAN [40], which matches the mean embedding of different domain distributions from different task-specific layers in CNN, and Zeillinger et al. [41] proposed to use means of order-wise moment differences to match the higher-order central moments of probability distributions. State-of-the-art guides knowledge transfer between domains while maintaining consistency of the relevant semantics before and after adaptation [42]. Class-level distribution alignment across the source and target domains was achieved using the Easy-to-Hard Transfer Strategy and a Prototype Feature Alignment Network [43]. The idea of using an intermediate domain [37] to perform unsupervised domain adaptation was effective in consumer image, which encourages us to apply the idea in satellite image dataset settings. Also, Saito et al. [38] show domain adaptation should not be rigorous and uniform in every pipeline phase, and careful inspection is required to design the domain adaptation pipeline to achieve optimal results.

Contrastive Learning for Domain Adaptation Domain Adaptation requires producing uniform or domain-invariant features across domains. Lately, contrastive learning [44] in domain adaptation has gained much attention due to its straightforward work process to produce similar features across domains. However, it maintains discriminating characteristics in feature space to represent different classes in a singular domain. It uses a similarity function such as cosine similarity or Euclidean distance to measure the similarity between two vectors. Then it represents the image features in the domain invariant feature space [45, 46]. Contrastive learning is successful not only in single-source domain adaptation but also in multi-source domain adaptation [47]. Kang et al. [47] takes into account class information and uses the K-means clustering method to label the target dataset. Kalantidis et al. [48] argue that some important aspects of contrastive learning are not taken into account earlier. They used *hard negative mixing* strategy to use better the effect of negative samples with very minimum overhead computation.

3 Small Object Detection

The size of the satellite image is up to 400 million pixels, and object sizes are often less than 100 pixels. A typical satellite image patch is 1024×1024 or 1.05 million pixels. If an object is 10×10 or 100 pixels, the object's size is < 0.0001 of the area of the image. The success of object detection depends on how reliable the pixel- and object-feature extraction and region-proposal network in the DNN architecture is. The increased number of very small, densely packed objects in the image increases the chance of losing pixel-level feature information during the feature extraction phase. The RPN-based proposal network misses many small objects in the early stage of the processing pipeline and cannot be

recovered in the detection stage [49]. Moreover, the objects are very densely packed, and surrounding information will add extra noise as input and incur more post-processing operations.

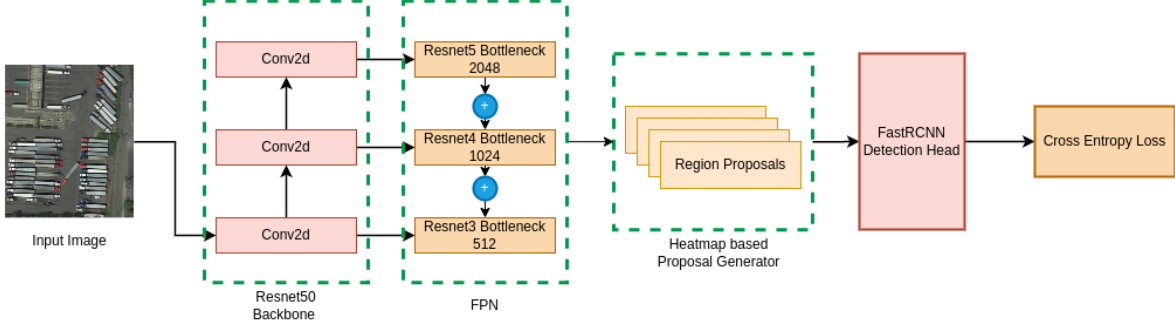


Figure 2: *Base*: Heatmap based multi-stage small object detection model used as a baseline [26]

3.1 Baseline Model for SOD

Base model is illustrated in Figure 2 and it is based on the pipeline proposed in [26]. The *Base* model has three parts: Backbone, Region Proposal Network (RPN), and Detection Head, and we have optimized the image load size, number of output channels per CNN block, and IOU in FastRCNN Detection Head parameters for the overhead dataset application. **Backbone** combines ResNet50 [26] as a feature extractor and the feature pyramid network (FPN) for multi-scale prediction. The residual connection efficiently combines features from previous layers with skip connections [27]. The residual block architecture allows for a deeper model without the vanishing-gradient effect. ResNet50 [26] achieves state-of-the-art performance in COCO [1] and LVIS [23] data sets. The FPN layer extracts three different scales of features from different layers of the backbone network, as illustrated in the FPN block in Figure 2. The Resnet3, Resnet4 and Resnet5 blocks represent strides of 8, 16, and 32 in the network. **Region Proposal Network (RPN)** in the *Base* model is a heatmap-based network that uses probabilistic region proposals based on the Gaussian kernels at different scales of features outputted by the FPN [8]. The element-wise comparison between the max-pool input and the output of the Gaussian kernel produces heat-maps in the image. The max-pool operation will elevate each pixel in the feature, except for the local maxima, where the value is 1. Each peak in the heat map corresponds to a center point of the object, as illustrated in Fig. 4(b) and (d). The image features at each key-point are used to predict the height and width of each object, and the resulting regressed bounding boxes are shown to perform well when objects are close to each other and overlap [26]. For the overhead imagery, the baseline model needs better *image augmentation* and *feature extraction* methods along with a higher number of *proposals per image*, and *detection per image* for reliable performance. **Detection Head** is adapted from the Faster-RCNN detector[24]. The detection head takes the filtered region proposals from the RPN module as input. The first task in the detection head is to convert each proposal into 7×7 pixel size grids with the same number of channels using the region-of-interest (ROI) pooler. Then, the pooling layer output is flattened and fed into the fully connected network (FCN) layers for the final detection output of (N, C) class predictor for C classes and N region proposals, and $(N, 4)$ bounding boxes [24].

3.2 Small Object Detection pipeline

Our small object detection *SOD* model [50] is an improvement over *Base* model as the pipeline is tuned to the small object detection. The backbone is now the Cross-Stage-Partial(CSP) Darknet backbone [20], and we have added the *Difficulty Estimation* block. We have changed the cross-entropy loss with a modified version of focal loss as illustrated in Figure 3. The efficiency of the region proposal network (*RPN*) module depends on the effectiveness of the backbone module. If the backbone fails to extract meaningful features for the small object in the image, the *RPN* module will likely fail to include the small object in the region proposals. Our findings show that 75% of the proposals from *RPN* modules in *Base* model tend to be trivial and frequent objects, such as backgrounds and partial object patches, as illustrated in Figure 4(b) and Figure 4(b) and explained in [50]. The first improvement was using the CSP **darknet backbone** network as it preserves better semantic information in the deeper layers of the convolutional neural network architecture [20, 51]. We have integrated the partial cross stage to provide the aggregation layer output at the low and the high resolution. Next, we replace the max-pooling layer with the spatial pyramid-pooling layer to accommodate for the finer feature extraction. The proposed small object detection model in Figure 3 concatenates layers 6 and 12, layers 4 and 16, layers 14 and 19 and layers 10 and 22, thus propagating the semantic information from the lower level to the higher level. The region proposal network considers the multi-resolution features from layers 17, 20, and 23 for

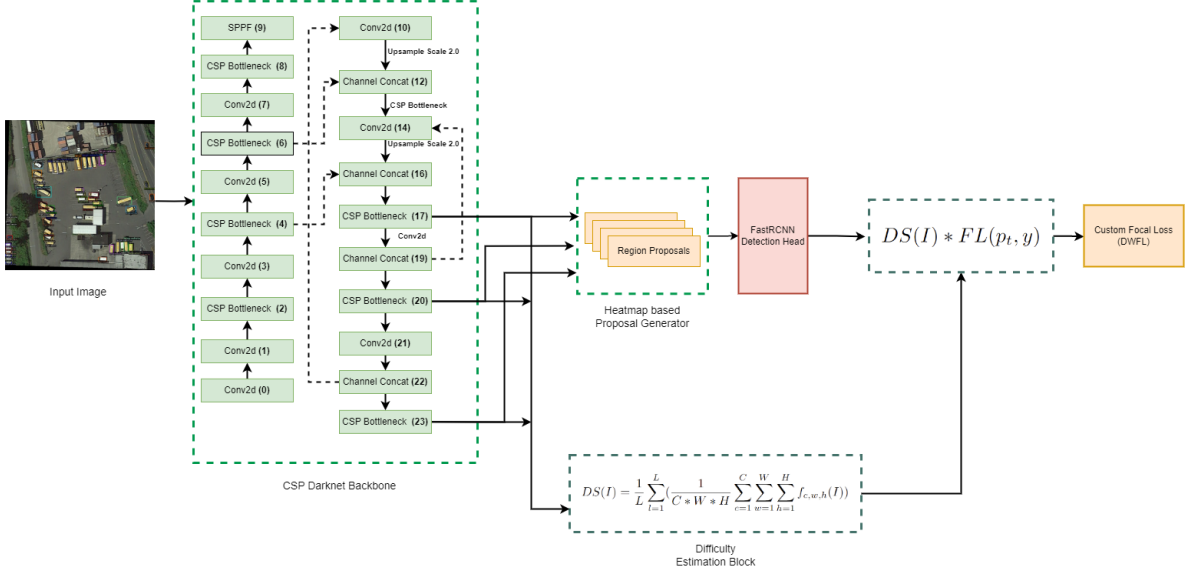


Figure 3: *SOD* model: Small Object Detection model with update backbone, new loss function, and the difficulty estimation block.

proposal generation, as illustrated in Figure 3. **Difficulty Estimator (DE)** module numerically captures the complexity of an image feature from the active neuron information of the network. It calculates the overall difficulty of each image as in [52]. The difficulty score (DS) for an FPN feature level with a resolution of $C \times W \times H$ for the image I is calculated in Eq. 1.

$$DS(I) = \frac{1}{L} \sum_{l=1}^L \left(\frac{1}{C * W * H} \sum_{c=1}^C \sum_{w=1}^W \sum_{h=1}^H f_{c,w,h}(I) \right) \quad (1)$$

The C , W , H are the feature output channels, the feature width, and the feature height, respectively, at any FPN level (l); L denotes the number of FPN levels used for difficulty calculation. $f_{c,w,h}(I)$ denotes the value of the sigmoid linear unit (SiLU) at all pixels in the image I . Using this block, we calculate the number of total neurons fired for a single image in the forward pass. We divide all activation values by the total dimension of the characteristic C , W , H to obtain the difficulty score (DS) at the FPN level. We derive this DS from 3 different levels of FPN and average the values to obtain the final DS for an image I . The increase in complexity for this DS block is nearly negligible. The Big Oh (O) notation for this block is $O(r)$, where r is the batch size in each iteration.

$$\forall c \in C, \alpha'_c = -1 * \log \left(\frac{|C_c|}{|C_1 \cup C_2 \cup \dots|} \right) \Rightarrow \alpha_c = \beta * \frac{\alpha'_c - \min(\alpha_c)}{\max(\alpha_c) - \min(\alpha_c)} \quad (2)$$

Custom Focal Loss is calculated from the difficulty scores for each image, and we propose replacing the loss of cross-entropy with the loss of custom focalization, as illustrated in Figure 3. The difficulty scores are calculated using equation 1 for each image by a difficulty estimator block as a weight factor to focus more on complex images with a high diversity of objects and a high variation in pixel-level features. The basic form of the focal loss function is outlined in equation 3.

$$FL(p_t, y) = \alpha_t * (1 - p_t)^\gamma * CE(p, y) \quad DWFL(x, p_t, y) = DS(I) * FL(p_t, y), \quad (3)$$

The p_t is the probability distribution of the target t , and y is the ground truth of the object being a specific class, γ is the modulating factor, α_t is used as a weighting factor, and CE represents the cross-entropy function. We propose a new measure, the Difficulty Weighted Focal Loss (DWFL) in equation 3 as a product of difficulty score, $DS(I)$ in Eq. 1, and focal loss for the image, $FL(p_t, y)$ in Eq. 3. The value α is used in the $FL(p_t, y)$ calculation to control the class imbalance problem in our source and target data sets. The α_c is calculated as in Eq. 2 for each class, where the modulating factor α'_c depends on the frequency $|C_c|$ of a particular class in the data set and $|C_1 \cup C_2 \cup C_3 \dots|$ is the total number of all instances of all classes in the data set. The normalized α_c values from Eq. 2 are used across different classes c , $c \in C$ to mitigate the imbalance of object class labels. In the experiment section 5 we confirm that the proposed normalization of α_c in Eq. 2 is more effective and gives a stable loss calculation for a highly unbalanced class count in the data set.

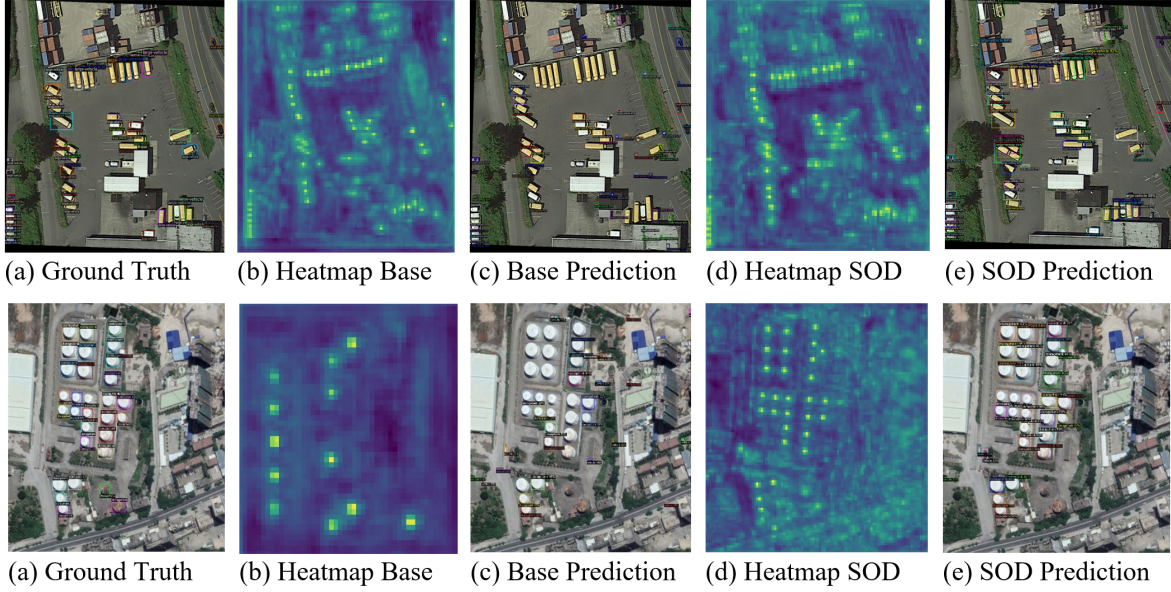


Figure 4: Proposals and detection results from the *Base* and *SOD* model for DOTA2.0(Target) and DIOR (Source) datasets.

4 Domain Adaptation Methods

Different overhead image datasets are usually taken at different geographical locations, and different types of satellites were used to capture images with different orientations under various weather and lighting conditions. There is a handful of annotated overhead image collections [53], and they all have different object class annotations, both in terms of frequency and assigned object labels. This contributes to a large domain gap between our source and target data sets. The performance of object detection on target degrades drastically when the domain gap is very w.r.t source dataset. Domain adaptation (DA) methods are key to the solution to this problem. Using domain adaptation methods, we can perform better in unseen datasets not introduced during the training phase. The goal of the self-supervised or unsupervised domain adaptation is to produce invariant features for a particular class across domains. In the experiment section 5 we confirm that the domain adaptation of the source in the training process improves the object detection performance.

4.1 HeatDA model: Heat Domain Adaptation Model

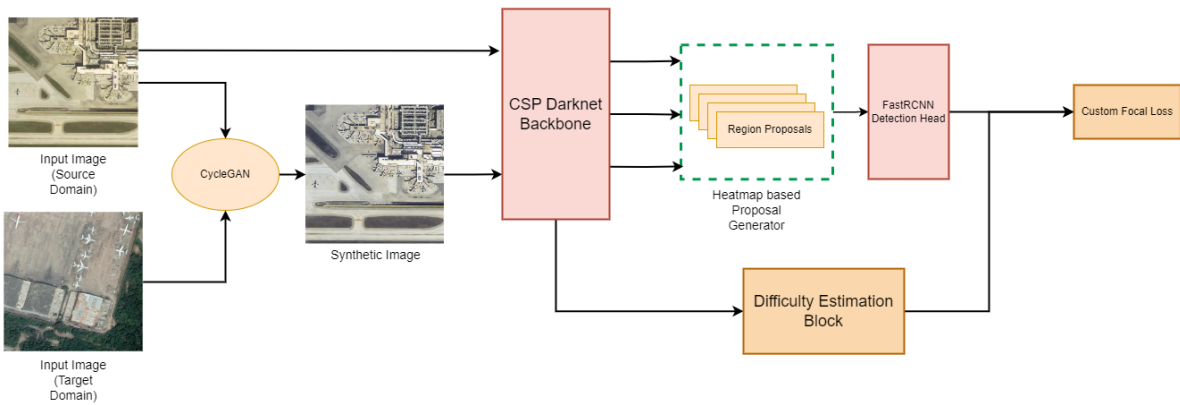


Figure 5: *HeatDA*: Heat Domain Adaptation model with pre-processed translated image domain adaptation.

Here, we propose a pre-processing step for the pipeline outlined in Figure 3 and map the source domain into the target domain first, as illustrated in Figure 5, as we have found that closing the source and target gap using progressive domain

adaptation leads to better object detection in the previously unseen overhead imagery. We train the CycleGAN domain discriminator [18, 54] using source and target image examples. The resulting domain discriminator model translates the source image to the target domain, as illustrated below in Figure 9. This additional CycleGAN domain discriminator model illustrated in Figure 5 allows us to align pixel-level features between two domains and use the original source image and the translated source image to train the SOD network, as illustrated in Figure 5. The conversion of the source to the target domain allows us to incorporate target-like domain characteristics without relying on the object-level annotations that might or might not be present. Training the *HeatDA* using target-like images helps to align pixel-level semantic information for the source and target domain, thus improving the detection performance.

4.2 LGDA Model: Local Global Domain Adaptation Model

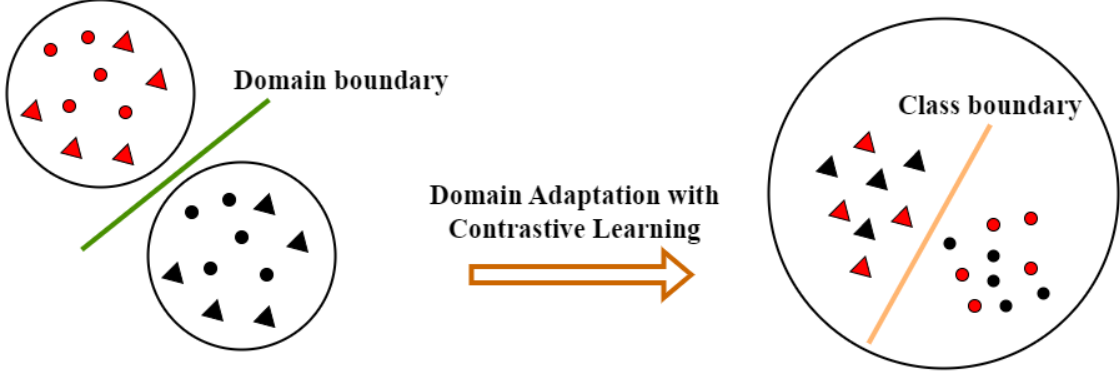


Figure 6: Domain Adaptation with contrastive learning. Left-side of the arrow shows feature space (circles) before Domain Adaptation and the right side shows after Domain Adaptation. Here, different colors indicate different domain distributions, and the different shapes represent different classes in a domain.

Contrastive learning [44, 45] is a simple process of measuring pair-to-pair relationships based on the similarities between different pairs, such as query-positive or query-negative. The functional strategy of contrastive loss is illustrated in Figure 6. Feature representation of the source and target objects differs in the feature space, and there is a huge gap due to lightning, geographic, weather, and acquisition differences, and the difference is illustrated by a green line in Figure 6. Contrastive learning brings similar points to close together and pushes dissimilar points separate from each other by calculating similarities between pairs [47, 16]. A pair of feature vectors with high similarity are placed close together, and vector pairs with low similarity are placed distantly in feature space. In the ideal case, the contrastive domain adaptation maps the feature space of the source dataset to the target dataset so that the features representing objects in the same class in the source and the target domain dataset are closer together. In this light, we propose to enforce contrastive learning on local features to minimize the domain gap with respect to the local characteristics in the image i.e. color and texture captured by deep features of the pixel and its nearest surroundings. Here, we produce domain-invariant object features for source and target domains by increasing similarities between *Query-Positive* pair and decreasing similarities between *Query-Negative* pairs. We introduce the Informative Noise Contrastive Estimation (InfoNCE) loss measure of finding similarities and dissimilarities between features in Equation 4. Similarity of two features u and v is captured by a cosine score $sim(u, v) = u^T / \|u\| \|v\|$. The *Query* is from the source, the *Positive* example is from the translated source domain denoted as SaT in Figure 7, and negative examples are with different classes than the *Query* example and from the target domain. Contrastive learning increases the similarity between *Query* and the *Positive* sample and increases the dissimilarity between *Query* and N negative samples $Negative_n, n \in [1, N]$ as outlined in Eq. 4.

$$InfoNCE = -\log \frac{\exp(sim(Query, Positive)/\tau)}{\sum_{n=1}^N \exp(sim(Query, Negative_n)/\tau)} \quad (4)$$

The Informative Noise Contrastive Estimation (InfoNCE) loss measure is low when the similarity between the *Query* and the *Positive* example is high and when then the similarity between *Query* to all *Negative* examples is low. Using this loss, we are learning domain invariant features. N is the mini-batch size during the training phase, and τ is the temperature that controls the strength of penalties in hard negative samples. Our implementation ensures that we find a similar example as *Positive* case and dissimilar examples as *Negative* cases. Figure 7 illustrates the proposed Local Global Domain Adaptation *LGDA* model and incorporates the proposed approach in the small object detection framework. This architecture focuses on performing domain adaptation on a highly class-label imbalance dataset where labeled objects are small compared to the image size. We added two modules to two new modules: Local Feature

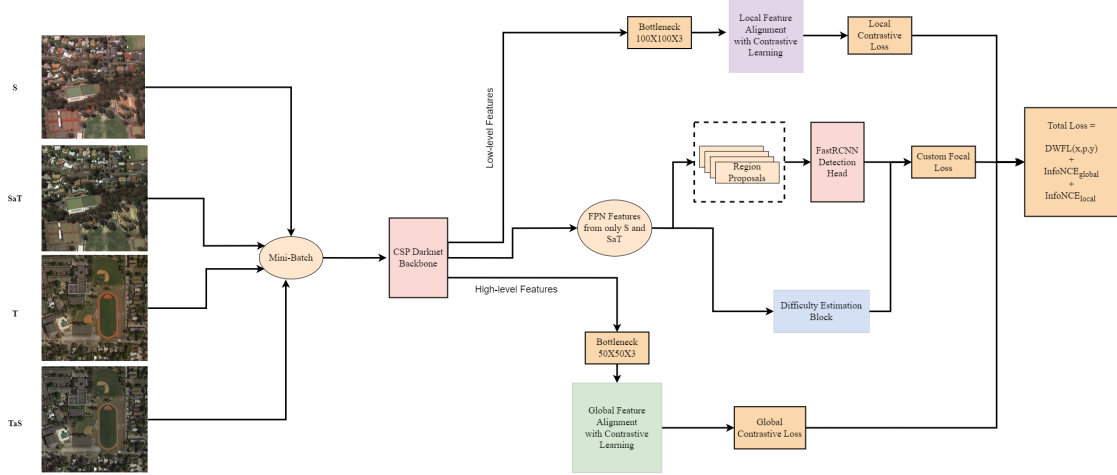


Figure 7: Local and Global Domain Adaptation(LGDA) model with contrastive learning.

Alignment and Global Feature Alignment for contrastive learning. Our proposed model takes input from four different distributions, among them, two are the source and target domains, and the other two are new intermediate domains, Source as Target (SaT) and Target as Source(TaS), from the source and target datasets, respectively, generated from the CycleGAN [18] network to reduce the gap between the source (S) and target (T) domains.

As shown in Figure 7, mini-batch inputs are passed into *CSP DarkNet* backbone. Next, features extracted from the *CSP DarkNet* backbone are fed into Local Feature Alignment and Global Feature Alignment modules for calculating *Local Contrastive Loss* and *Global Contrastive Loss*, respectively. However, RPN produces region proposals for object detection tasks from only S and SaT domain features passed from the backbone because we have ground truth for these two domains. The later part of the architecture is a traditional RCNN-style object detector with classification and regression modules.

Local Domain Adaptation focuses on the local features in an image and assumes there is no ground truth object labeling for the target dataset, only for the source dataset. Local features capture low-level descriptions of a pixel and its neighbors in an image. The images from a mini-batch pass through the backbone and local features are saved from the earlier layers of the backbone. The saved local features are in the shape of $256 \times 100 \times 100$, where dimensions are in the form of C, W, H, respectively. To reduce the necessity of computational power and GPU memory and improve similarity computation performance, we pass the features into the bottleneck module as shown in Figure 7 and downgrade the shape to $3 \times 100 \times 100$. In Figure 7, S and T are images drawn from the source and target datasets, respectively, where SaT and TaS are the corresponding images of S and T in translated form, produced by the CycleGAN network. Let us denote the local feature vectors from S, SaT, T and TaS as L_k^S , L_k^{SaT} , L_k^T , and L_k^{TaS} , respectively. Where k is the index of the mini-batch. For the adaptation of the S and SaT domain, we select a local feature $L_i^S \in L^S$ as a query and the corresponding feature from $L_i^{SaT} \in L^{SaT}$ as the positive case. Negative cases are all other local characteristics $L_j^{SaT} \in L^{SaT}$, where $j \neq i$.

$$InfoNCE_{local}^{S,SaT} = -\log \frac{\exp(\text{sim}(L_i^S, L_i^{SaT})/\tau)}{\sum_{j=1}^N \exp(\text{sim}(L_i^S, L_j^{SaT})/\tau)} - \log \frac{\exp(\text{sim}(L_i^{SaT}, L_i^S)/\tau)}{\sum_{j=1}^N \exp(\text{sim}(L_i^{SaT}, L_j^S)/\tau)}, j \neq i \quad (5)$$

$$InfoNCE_{local}^{T,TaS} = -\log \frac{\exp(\text{sim}(L_i^T, L_i^{TaS})/\tau)}{\sum_{j=1}^N \exp(\text{sim}(L_i^T, L_j^{TaS})/\tau)} - \log \frac{\exp(\text{sim}(L_i^{TaS}, L_i^T)/\tau)}{\sum_{j=1}^N \exp(\text{sim}(L_i^{TaS}, L_j^T)/\tau)}, j \neq i \quad (6)$$

After accumulating loss for all query images in a minibatch, the total bidirectional local domain adaptation loss can be formulated as follows.

$$InfoNCE_{local} = InfoNCE_{local}^{S,SaT} + InfoNCE_{local}^{T,TaS} \quad (7)$$

Global Domain Adaptation relies on the global feature alignment between the source and the target dataset. The global features represent a more abstract formation of objects present in the image and are saved from the last layer of the backbone. The shape of the global features is $256 \times 25 \times 25$, where the dimensions are C, W, and H, respectively. Again, the same as for local features, we use a bottleneck module to reduce the size of global features to $3 \times 25 \times 25$. Global features are high-level features in the DNN pipeline. Global domain adaptation and feature alignment are also performed at the mini-batch level to restrict computational and GPU memory expense.

The global feature vectors of training mini-batch input: S , SaT , T and TaS are indexed as G_k^S , G_k^{SaT} , G_k^T and G_k^{TaS} , where k is the index of the mini-batch. The global contrastive loss for S and SaT is calculated by selecting a query sample $G_i^S \in G^S$ and a positive case from the corresponding image feature $L_i^{SaT} \in L^{SaT}$ and vice versa. We take the negative cases as all the other global features $G_j^{SaT} \in G^{SaT}$, where $j \neq i$, and the adaptation formula for S and SaT domains in global feature space is outlined in Eq. 8.

$$InfoNCE_{global}^{S,SaT} = -\log \frac{\exp(\text{sim}(G_i^S, G_i^{SaT})/\tau)}{\sum_{j=1}^N \exp(\text{sim}(G_i^S, G_j^{SaT})/\tau)} - \log \frac{\exp(\text{sim}(G_i^{SaT}, G_i^S)/\tau)}{\sum_{j=1}^N \exp(\text{sim}(G_i^{SaT}, G_j^S)/\tau)}, j \neq i \quad (8)$$

The adaptation formula for T and TaS domains in global feature space is outlined in Eq. 9.

$$InfoNCE_{global}^{T,TaS} = -\log \frac{\exp(\text{sim}(G_i^T, G_i^{TaS})/\tau)}{\sum_{j=1}^N \exp(\text{sim}(G_i^T, G_j^{TaS})/\tau)} - \log \frac{\exp(\text{sim}(G_i^{TaS}, G_i^T)/\tau)}{\sum_{j=1}^N \exp(\text{sim}(G_i^{TaS}, G_j^T)/\tau)}, j \neq i \quad (9)$$

The accumulated global domain adaptation loss in a mini-batch is now calculated in Eq. 10.

$$InfoNCE_{global} = InfoNCE_{global}^{S,SaT} + InfoNCE_{global}^{T,TaS} \quad (10)$$

Finally, the *LGDA* model combines the local and the global contrastive loss with the detection loss, and the final loss function is now calculated as in Eq. 11:

$$TotalLoss = InfoNCE_{global} + InfoNCE_{local} + DWFL(x, p, y) \quad (11)$$

5 Experiments

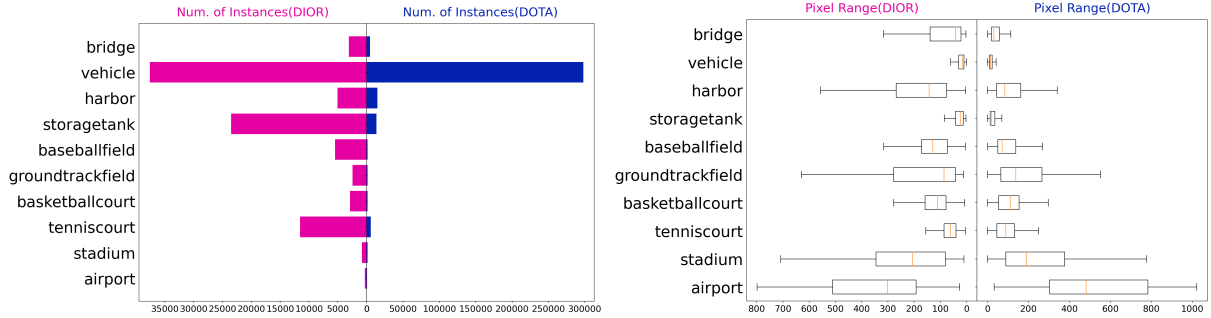


Figure 8: Class instances and object pixel size distribution for the DIOR and DOTA2.0 data set.

5.1 Datasets

We evaluated the proposed approach in the two largest annotated satellite image collections, DIOR [2], and DOTA2.0 [14]. DIOR is the dataset for the source domain, and we used the ground-truth annotation for DIOR in our detection module and model evaluation. DOTA2.0 is the target dataset that is used to adapt to the local and global domain, as illustrated in Figure 8. We assume that the DOTA2.0 annotations are unavailable at the object detection time and use ground truth to evaluate the system’s performance. We kept only common classes available in the DIOR and DOTA2.0 datasets in our experiments and assigned the same class label to each corresponding class in both datasets, as illustrated for the reduced DIOR dataset and the reduced DOTA2.0 dataset in Figure 8

The original **DIOR** dataset consists of 24,500 Google Earth images of areas in 80 countries, but after picking only common classes, the reduced DIOR has 11,402 images. The quality of the images varies, and the content was captured during multiple seasons and weather conditions. The data set covers a wide range of spatial resolutions, object size, object orientation variability, and a diverse class distribution, as illustrated in Fig. 8. The spatial resolution of the images is in the range $[0.5m, 30m]$, and the size of the images in the data set is 800×800 pixels. The number of annotated objects in the data set is 97,450 and is classified into 10 classes [2]. The number of images in the training set is 10,888; in the testing set, we have 512 images.

The DOTA2.0 dataset consists of 2,430 overhead image images collected from Google Earth, the Gaofen-2 (GF-2) satellite, and the Jilin-1 (JL-1) satellite [14]. The image sizes in the data set range from 800×800 to $29,200 \times 27,620$ pixels. The GSD range in the DOTA2.0 dataset is 0.1 to 0.87 m, and the average number of objects per image is 220.

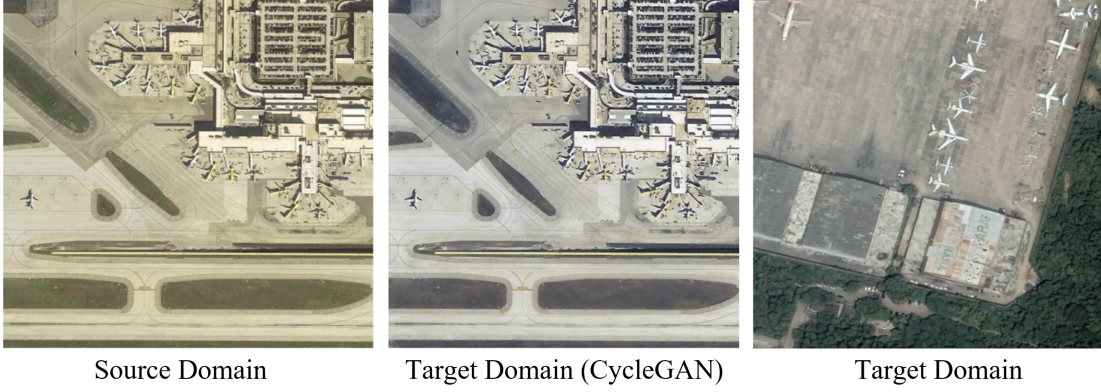


Figure 9: Domain translation from S to SaT using CycleGAN [18]: (a) source domain(S), (b) CycleGAN generated target domain(SaT), and (c) target domain(T).

In the experiment, we split large images into sub-images of size 1024×1024 pixels with an overlap of 200 pixels. After splitting, we get 23,300 images from the original DOTA2.0 dataset. After selecting only common classes, the reduced version of the DOTA2.0 training set has 11,551 images, and the validation set has 3,488 images classified into 10 classes.

5.2 Experimental Setup

Source as Target (SaT) and Target as Source (TaS) data for S (DOTA) and T (DIOR) are created using the PyTorch implementation of the CycleGAN [18, 54] network with the setup: the learning rate was 0.001; the number of training epochs was 2; load size was 800; and the crop size was 640.

The proposed model architecture *LGDA* is illustrated in Figure 7 and is described in Section 4.2. On the other hand, the model *SOD* is the small object detection pipeline, an extension of the Base [26] model. Two proposed models *HeatDA* and *LGDA* are integrated as an extension of the model *SOD*.

The loss of InfoNCE in Equation 4 requires the same image from different domains as in the query and in the positive case. To achieve this goal, we created a custom data loader in PyTorch that fetches the exact image of the different domains in a mini-batch. This custom data loader ensures that we get Query and Positive examples inside a mini-batch during the training. In our experiments, eight is the size of the mini-batch, and the $8 \times 4 = 32$ images were fed into the *LGDA* model in each mini-batch. The number of negative cases and the temperature were set to 7 and 0.12, respectively, for contrastive learning. Our research found that passing the S and SaT for the object detection task during the full training time makes the model over-fitted to the source domain. To eliminate this problem, we implemented random sample selection, which randomly selects 8 of 16 images from S and SaT and passed them on to the object detection module. Li et al. [55], as well as our experiments, found that Global Average Pooling (GAP) loses a significant amount of important context information when working with satellite images, so we replace GAP with the bottleneck module for channel reduction. Finally, all experiments were carried out with the NVIDIA 2 x RTX 6000 GPU with 49GB of memory, 11th generation Intel® Core™ i9-11900K @ 3.50GHz \times 16 CPU, and 70GB of system memory.

5.3 Performance Measures

The performance of the *SOD* model for images with a highly dense object distribution is illustrated in Figure 4(e), as it captures more objects than the Base model and produces a higher number of proposals for small objects from the images that Base model missed.

$$\begin{aligned}
 P &= TP / (TP + FP), & R &= TP / (TP + FN), \\
 F1 &= \frac{2 * P * R}{P + R}, & & (12)
 \end{aligned}$$

$$AP = \sum_{k=0}^{k=n-1} [R(k) - R(k+1)] * P(k),$$

$$mAP = \frac{1}{n} \sum_{k=1}^{k=n} AP(k)$$
(13)

The precision scores P , recall R , F1 score $F1$, and mean precision mAP are calculated in Eq. 12 and Eq. 13. True positives TP are outcomes that the model correctly predicted, false positives FP are outcomes that the model missed, and true negatives TN are outcomes that the model incorrectly predicted. All these metrics were calculated based on an IOU of 0.5: 0.95, and the number of proposals per image was set to 256. Precision P measures the fraction of relevant occurrences between recovered instances, and recall R is the fraction of objects that the model correctly identified among all relevant instances.

The $F1$ score provides a single measure of how well the model performs when given a class imbalance dataset, and mAP is computed as shown in Eq. 13, where n is the number of classes in the test set, and $AP(k)$ is the Average Precision (AP) of class k in the test set. Here, AP is the weighted sum of precision at each threshold (n is the number of thresholds), and the weight is the increase in recall (Eq. 13).

5.4 Object Detection Comparisons

Adapting the local domain helped us align the pixel-level characteristics in the source and target domains. Before adaptation of the local domain, there were a few centroids of local feature distribution in the feature space. Still, after alignment of the feature using the adaptation of the local domain, both the source and target domains share the uniform center of the pixel-level features in the feature space and an improvement in performance in the target domain dataset, as illustrated in Table 2 and Figures 10 (a)-(d). Therefore, without using the ground truth annotation for the target dataset, *SOD* model detects a higher number of objects than the *Base* model [50]. The improvement in proposal generation is illustrated in Figure 4(d) and Figure 4(d), and the detection result can be seen in Figure 4(e) and Figure 4(e). The range of α'_c values in the DIOR dataset is 0.2 to 0.79 and the range of α'_c values in the DOTA2.0 dataset is 0.15 to 0.96, which represents a very tight scaling factor for FL in both data sets.

Table 1: Class-wise AP and overall mAP from *SOD*, *HeatDA*, and *LGDA* model for DIOR and DOTA2.0dataset.

DIOR	mAP	Bridge	Vehicle	Harbor	Storage	Baseball	Track	Basketball	Tennis	Stadium	Airport
					Tank	Field	Field	Court	Court		
No. labels	NA	176	2079	254	2623	250	138	171	580	40	8
SOD	56.2	31.86	39.65	51.08	53.41	83.80	57.39	76.44	82.57	55.21	29.5
HeatDA	58.2	37.45	42.78	53.70	54.21	82.71	57.20	76.12	84.42	58.64	37.10
LGDA	61.8	40.84	44.85	55.72	57.40	87.63	62.35	79.22	86.27	61.51	38.32
DOTA2.0	mAP	Bridge	Vehicle	Harbor	Storage	Baseball	Track	Basketball	Tennis	Stadium	Airport
					Tank	Field	Field	Court	Court		
No Labels	NA	1040	85469	5711	5417	516	417	358	1662	393	154
SOD	18.2	7.18	7.68	14.36	27.52	16.70	15.23	23.64	65.32	4.58	7.40
HeatDA	20.4	8.51	9.33	15.84	28.20	17.87	18.24	23.18	62.10	6.65	10.81
LGDA	22.2	9.23	9.89	17.74	30.82	19.64	18.18	27.29	68.80	7.23	12.88

For domain adaptation learning, we have considered DIOR as the source dataset and DOTA2.0 as the target dataset. It was assumed that there is no ground-truth annotation for the target dataset, and we have ground-truth access only to the DIOR source dataset. To create a baseline result, we trained the *SOD* model with DIOR and DOTA2.0 ground truth data sets, and the evaluation was carried out with the corresponding validation set. Again, while evaluating proposed *HeatDA* and *LGDA* models, we trained using only the annotation of the source data set, but the evaluation was carried out on both the source and target data sets.

Table 2: Comparison of Precision, Recall, and F1 score between different models on the source and target domains.

	SOD			HeatDA			LGDA		
Dataset	Precision	Recall	F1	Precision	Recall	F1	Precision	Recall	F1
DIOR	56.9	62.8	58.9	58.7	63.9	60.1	62.8	66.8	63.9
DOTA2.0	18.3	35.7	25.1	20.8	37.4	27.2	22.3	39.9	29.1

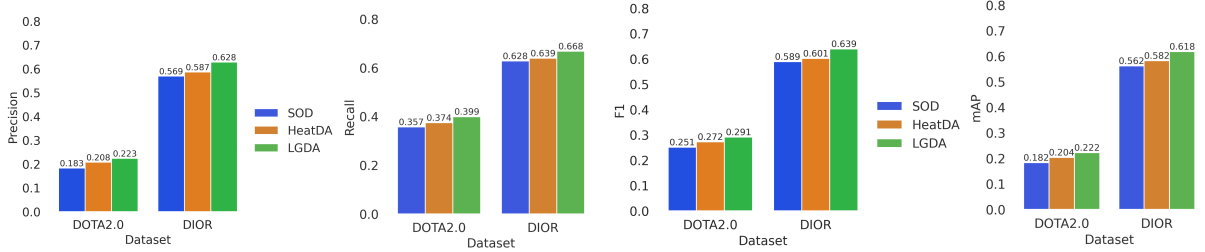


Figure 10: (a) Precision (b) Recall (c) F1 Score and (d) mAP comparison from different models vs different datasets (IOU=0.50:0.95).

Precision of three models in three different data sets are illustrated in Figure 10(a). In the ten classes, the average precision of the *SOD* model is 56.9% and 18.3% for the DIOR and DOTA2.0 datasets, respectively. *HeatDA* model shows a reasonable improvement in the target dataset with the help of translated image training. Figure 10(a) shows an improvement in AP of 2.5% for DOTA2.0 and 1.8% for the DIOR data set. The improvement in the *HeatDA* model is significant for classes with small objects and difficult to distinguish. However, after using contrastive learning to adapt local and global domains, our model *LGDA* shows a 5.9% and 4.0% increase in precision compared to the model *SOD* for the DIOR and DOTA2.0 datasets, respectively. **Recall** of three models in different data sets are illustrated in Figure 10(b). The recall models with *SOD* for the source and target data sets are, respectively, 62.8% and 35.7%. The *LGDA* model with domain adaptation significantly improved all data sets. The recall measure for the target data set was 4.3% higher than the *SOD* model (see Figure 10(b)). The **F1 Score** of the three models is illustrated in Figure 10(c). The F1 score found in the *LGDA* model for the target data set increased by 4.0% compared to the model *SOD*. For the *HeatDA* model, the improvement for different data sets was also remarkably significant and comparable to the current baseline findings. The **mAP** in the classes for different datasets and models is presented in 10(d). The mAP for source data, when trained on source data, is 56.2% for the *SOD* model and 61.8% for the *LGDA* model, a 5.6% increase as illustrated in 10(d). The mAP for the target data, when trained on the target dataset, is 18.2% for the *SOD* model and 20.4% for the *HeatDA* model, a 2.2% increase 10(d). An overall comparison is also presented in Table 2, where the bold text shows the best outcome from the *LGDA* model on both source and target datasets. The best result for the target data set was achieved from the *LGDA* model after performing the local and global domain adaptation in our proposed *LGDA* model. Table 2 and Figure 10(d) show a 4.0% increase in mAP compared to the *SOD* model.

We performed an ablation study to achieve our best results in the target domain dataset, as shown in Figure 10. The summary of the ablation study is illustrated in Figure 11 based on three key hyperparameters. First, we look for the optimal value for the number of negative examples, as shown in Figure 11(a). We started our experiments with a value of 2, and we can see that the model did not perform well with fewer negative examples in contrastive loss. To generalize learning, we increased the value to 7 and recorded our best performance in the target dataset. Increasing the negative examples further did not help us to learn because of the imbalanced nature of the data set. Our target dataset is dominated by the vehicle class, as shown in Figure 8(right). Increasing the number of negative examples also

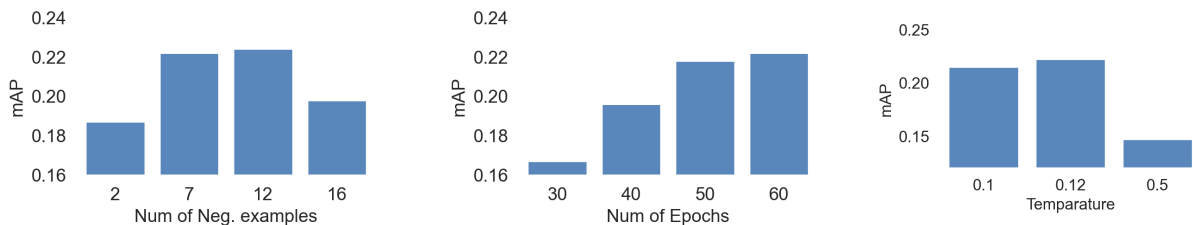


Figure 11: Ablation Study: (a) mAP vs. Negative Examples, (b) mAP vs. Epochs, and (c) mAP vs. Temperature.

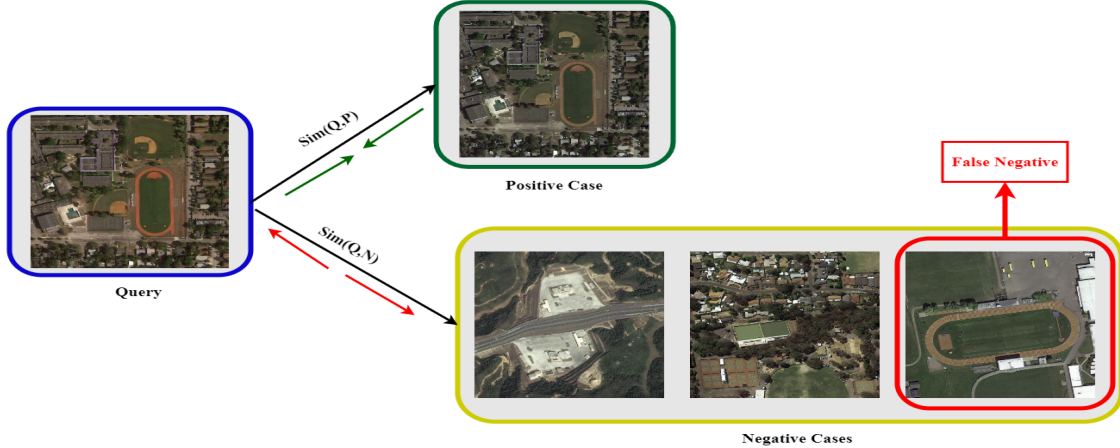


Figure 12: Example of False Negative occurrence in a highly imbalanced dataset.

increases the chances of getting false negative (FN) examples, as shown in Figure 12 in contrastive learning. In highly imbalanced datasets such as DOTA, the FN example makes the model biased toward a certain class, and the model’s overall performance degrades significantly. The adverse effect of bias is evident in Figure 11(a) when trained with 16 negative examples. After careful inspection and to reduce computational expense, we set the number of negative examples equal to 7.

Second, our baseline model was trained for 30 epochs to record the SOT result. But our LGDA model was trained for 20 more epochs as we added two more loss functions for contrastive learning. As illustrated in Figure 11(b), our experiments found that training for more epochs does not significantly improve performance. Therefore, all results were recorded with 50 training epochs. Lastly, the temperature value in contrastive loss is very sensitive, and small changes in value can drastically change the result. This is evident in Figure 11(c), placing a 50% penalty on contrastive loss dramatically reduces performance, and using a 12% penalty shows the optimal result.

6 Conclusion and Future Work

Object detection in aerial images is one of the most challenging tasks in computer vision research because many small and overlapped objects exist in the images. The success of DNN object localization depends on a large amount of annotated training data and a reliable feature extractor module in the pipeline. In this paper, we present a strong feature extractor that captures balanced low-level and high-level features for small objects. Next, we present the heat-map-based region proposal module to capture small objects better. The domain gap in satellite images is larger than that in consumer images because of weather conditions, geographic changes, and camera orientations. We perform progressive domain alignment by creating two intermediate domains, w.r.t. source, and target datasets. We show the effect of processive domain adaptation in Figures 9. The proposed method *HeatDA* performed extremely well with more than 60% mAP for several classes such as *storage tank*, *airplane*, and *storagetank* in the DIOR data set. We also use contrastive learning to adapt to local and global domains. Careful selection of the training pipeline, the number of negative samples, the downsampling strategy, and the temperature value can improve the effectiveness of contrastive learning. Our proposed *LGDA* model outperformed the *SOD* model in the target data set by 4%, 4.3%, & 4% for precision, recall, and mAP metrics, respectively. Next, we plan clustering-based pseudo-labeled for target domain objects, debiased instance-level Domain Adaptation, and unknown class discovery for satellite images.

References

- [1] Tsung-Yi Lin, Michael Maire, Serge Belongie, James Hays, Pietro Perona, Deva Ramanan, Piotr Dollár, and C Lawrence Zitnick. Microsoft coco: Common objects in context. In *European conference on computer vision*, pages 740–755. Springer, 2014.
- [2] Ke Li, Gang Wan, Gong Cheng, Liqiu Meng, and Junwei Han. Object detection in optical remote sensing images: A survey and a new benchmark. *ISPRS Journal of Photogrammetry and Remote Sensing*, 159:296–307, 2020.
- [3] João Valente, Bilal Sari, Lammert Kooistra, Henk Kramer, and Sander Múcher. Automated crop plant counting from very high-resolution aerial imagery. *Precision Agriculture*, 21(6):1366–1384, 2020.

- [4] Scott Workman and Nathan Jacobs. Dynamic traffic modeling from overhead imagery. In *Proceedings of the IEEE/CVF Conference on Computer Vision and Pattern Recognition*, pages 12315–12324, 2020.
- [5] Debojyoti Biswas, M M Mahabubur Rahman, Ziliang Zong, and Jelena Tešić. Improving the energy efficiency of real-time dnn object detection via compression, transfer learning, and scale prediction. In *2022 IEEE International Conference on Networking, Architecture and Storage (NAS)*, pages 1–8, 2022.
- [6] Jia Liu, Jianjian Xiang, Yongjun Jin, Renhua Liu, Jining Yan, and Lizhe Wang. Boost precision agriculture with unmanned aerial vehicle remote sensing and edge intelligence: A survey. *Remote Sensing*, 13(21):4387, 2021.
- [7] Xiang Long, Kaipeng Deng, Guanzhong Wang, Yang Zhang, Qingqing Dang, Yuan Gao, Hui Shen, Jianguo Ren, Shumin Han, Errui Ding, et al. Pp-yolo: An effective and efficient implementation of object detector. *arXiv preprint arXiv:2007.12099*, 2020.
- [8] Xingyi Zhou, Dequan Wang, and Philipp Krähenbühl. Objects as points. *arXiv preprint arXiv:1904.07850*, 2019.
- [9] Tsung-Yi Lin, Priya Goyal, Ross Girshick, Kaiming He, and Piotr Dollár. Focal loss for dense object detection. In *Proceedings of the IEEE international conference on computer vision*, pages 2980–2988, 2017.
- [10] Payal Mittal, Raman Singh, and Akashdeep Sharma. Deep learning-based object detection in low-altitude uav datasets: A survey. *Image and Vision computing*, 104:104046, 2020.
- [11] Srishti Srivastava, Sarthak Narayan, and Sparsh Mittal. A survey of deep learning techniques for vehicle detection from uav images. *Journal of Systems Architecture*, page 102152, 2021.
- [12] Xingkui Zhu, Shuchang Lyu, Xu Wang, and Qi Zhao. Tph-yolov5: Improved yolov5 based on transformer prediction head for object detection on drone-captured scenarios. In *Proceedings of the IEEE/CVF International Conference on Computer Vision*, pages 2778–2788, 2021.
- [13] Darius Lam, Richard Kuzma, Kevin McGee, Samuel Dooley, Michael Laielli, Matthew Klaric, Yaroslav Bulatov, and Brendan McCord. xvnet: Objects in context in overhead imagery. *arXiv preprint arXiv:1802.07856*, 2018.
- [14] Jian Ding, Nan Xue, Gui-Song Xia, Xiang Bai, Wen Yang, Michael Yang, Serge Belongie, Jiebo Luo, Mihai Datcu, Marcello Pelillo, and Liangpei Zhang. Object detection in aerial images: A large-scale benchmark and challenges. *IEEE Transactions on Pattern Analysis and Machine Intelligence*, pages 1–1, 2021.
- [15] Pengfei Zhu, Longyin Wen, Xiao Bian, Haibin Ling, and Qinghua Hu. Vision meets drones: A challenge. *arXiv preprint arXiv:1804.07437*, 2018.
- [16] Ziwei Deng, Quan Kong, Naoto Akira, and Tomoaki Yoshinaga. Hierarchical contrastive adaptation for cross-domain object detection. *Machine Vision and Applications*, 33(4):1–13, 2022.
- [17] Yangguang Zhu, Xian Sun, Wenhui Diao, Hao Li, and Kun Fu. Rfa-net: Reconstructed feature alignment network for domain adaptation object detection in remote sensing imagery. *IEEE Journal of Selected Topics in Applied Earth Observations and Remote Sensing*, 15:5689–5703, 2022.
- [18] Jun-Yan Zhu, Taesung Park, Phillip Isola, and Alexei A Efros. Unpaired image-to-image translation using cycle-consistent adversarial networks. In *Computer Vision (ICCV), 2017 IEEE International Conference on*, 2017.
- [19] Joseph Redmon, Santosh Divvala, Ross Girshick, and Ali Farhadi. You only look once: Unified, real-time object detection. In *Proceedings of the IEEE conference on computer vision and pattern recognition*, pages 779–788, 2016.
- [20] Alexey Bochkovskiy, Chien-Yao Wang, and Hong-Yuan Mark Liao. Yolov4: Optimal speed and accuracy of object detection. *arXiv preprint arXiv:2004.10934*, 2020.
- [21] Yang Liu, Peng Sun, Nickolas Wergeles, and Yi Shang. A survey and performance evaluation of deep learning methods for small object detection. *Expert Systems with Applications*, 172:114602, 2021.
- [22] Du Jiang, Gongfa Li, Chong Tan, Li Huang, Ying Sun, and Jianyi Kong. Semantic segmentation for multiscale target based on object recognition using the improved faster-rcnn model. *Future Generation Computer Systems*, 123:94–104, 2021.
- [23] Agrim Gupta, Piotr Dollar, and Ross Girshick. Lvis: A dataset for large vocabulary instance segmentation. In *Proceedings of the IEEE/CVF conference on computer vision and pattern recognition*, pages 5356–5364, 2019.
- [24] Shaoqing Ren, Kaiming He, Ross Girshick, and Jian Sun. Faster r-cnn: Towards real-time object detection with region proposal networks. *Advances in neural information processing systems*, 28, 2015.
- [25] Kaiming He, Georgia Gkioxari, Piotr Dollár, and Ross Girshick. Mask r-cnn. In *Proceedings of the IEEE international conference on computer vision*, pages 2961–2969, 2017.
- [26] Xingyi Zhou, Vladlen Koltun, and Philipp Krähenbühl. Probabilistic two-stage detection. *arXiv preprint arXiv:2103.07461*, 2021.

- [27] Kaiming He, Xiangyu Zhang, Shaoqing Ren, and Jian Sun. Deep residual learning for image recognition. In *Proceedings of the IEEE conference on computer vision and pattern recognition*, pages 770–778, 2016.
- [28] Joseph Redmon and Ali Farhadi. Yolov3: An incremental improvement. *arXiv preprint arXiv:1804.02767*, 2018.
- [29] Tsung-Yi Lin, Piotr Dollár, Ross Girshick, Kaiming He, Bharath Hariharan, and Serge Belongie. Feature pyramid networks for object detection. In *Proceedings of the IEEE conference on computer vision and pattern recognition*, pages 2117–2125, 2017.
- [30] Linxiang Zhu, Feifei Lee, Jiawei Cai, Hongliu Yu, and Qiu Chen. An improved feature pyramid network for object detection. *Neurocomputing*, 483:127–139, 2022.
- [31] Zhenxing Liu, Xiaoning Song, Zhenhua Feng, Tianyang Xu, Xiaojun Wu, and Josef Kittler. Global context-aware feature extraction and visible feature enhancement for occlusion-invariant pedestrian detection in crowded scenes. *Neural Processing Letters*, pages 1–15, 2022.
- [32] Yulin Wu, Ke Zhang, Jingyu Wang, Yezi Wang, Qi Wang, and Xuelong Li. Gcwnet: A global context-weaving network for object detection in remote sensing images. *IEEE Transactions on Geoscience and Remote Sensing*, 60:1–12, 2022.
- [33] Yiping Gong, Zhifeng Xiao, Xiaowei Tan, Haigang Sui, Chuan Xu, Haiwang Duan, and Deren Li. Context-aware convolutional neural network for object detection in vhr remote sensing imagery. *IEEE Transactions on Geoscience and Remote Sensing*, 58(1):34–44, 2019.
- [34] Jin Zhang, Yanjiao Shi, Qing Zhang, Liu Cui, Ying Chen, and Yugen Yi. Attention guided contextual feature fusion network for salient object detection. *Image and Vision Computing*, 117:104337, 2022.
- [35] Jiaxu Leng, Yihui Ren, Wen Jiang, Xiaoding Sun, and Ye Wang. Realize your surroundings: Exploiting context information for small object detection. *Neurocomputing*, 433:287–299, 2021.
- [36] Yancheng Bai, Yongqiang Zhang, Mingli Ding, and Bernard Ghanem. Sod-mtgan: Small object detection via multi-task generative adversarial network. In *Proceedings of the European Conference on Computer Vision (ECCV)*, pages 206–221, 2018.
- [37] Han-Kai Hsu, Chun-Han Yao, Yi-Hsuan Tsai, Wei-Chih Hung, Hung-Yu Tseng, Maneesh Singh, and Ming-Hsuan Yang. Progressive domain adaptation for object detection. In *Proceedings of the IEEE/CVF winter conference on applications of computer vision*, pages 749–757, 2020.
- [38] Kuniaki Saito, Yoshitaka Ushiku, Tatsuya Harada, and Kate Saenko. Strong-weak distribution alignment for adaptive object detection. In *Proceedings of the IEEE/CVF Conference on Computer Vision and Pattern Recognition*, pages 6956–6965, 2019.
- [39] Jakaria Rabbi, Nilanjan Ray, Matthias Schubert, Subir Chowdhury, and Dennis Chao. Small-object detection in remote sensing images with end-to-end edge-enhanced gan and object detector network. *Remote Sensing*, 12(9):1432, 2020.
- [40] Mingsheng Long, Yue Cao, Jianmin Wang, and Michael Jordan. Learning transferable features with deep adaptation networks. In *International conference on machine learning*, pages 97–105. PMLR, 2015.
- [41] Werner Zellinger, Thomas Grubinger, Edwin Lughofer, Thomas Natschläger, and Susanne Saminger-Platz. Central moment discrepancy (cmd) for domain-invariant representation learning. *arXiv preprint arXiv:1702.08811*, 2017.
- [42] Judy Hoffman, Eric Tzeng, Taesung Park, Jun-Yan Zhu, Phillip Isola, Kate Saenko, Alexei Efros, and Trevor Darrell. Cycada: Cycle-consistent adversarial domain adaptation. In *International conference on machine learning*, pages 1989–1998. Pmlr, 2018.
- [43] Chaoqi Chen, Weiping Xie, Wenbing Huang, Yu Rong, Xinghao Ding, Yue Huang, Tingyang Xu, and Junzhou Huang. Progressive feature alignment for unsupervised domain adaptation. In *Proceedings of the IEEE/CVF conference on computer vision and pattern recognition*, pages 627–636, 2019.
- [44] Raia Hadsell, Sumit Chopra, and Yann LeCun. Dimensionality reduction by learning an invariant mapping. In *2006 IEEE Computer Society Conference on Computer Vision and Pattern Recognition (CVPR'06)*, volume 2, pages 1735–1742. IEEE, 2006.
- [45] Ting Chen, Simon Kornblith, Mohammad Norouzi, and Geoffrey Hinton. A simple framework for contrastive learning of visual representations. In *International conference on machine learning*, pages 1597–1607. PMLR, 2020.
- [46] R Devon Hjelm, Alex Fedorov, Samuel Lavoie-Marchildon, Karan Grewal, Phil Bachman, Adam Trischler, and Yoshua Bengio. Learning deep representations by mutual information estimation and maximization. *arXiv preprint arXiv:1808.06670*, 2018.

- [47] Guoliang Kang, Lu Jiang, Yunchao Wei, Yi Yang, and Alexander Hauptmann. Contrastive adaptation network for single-and multi-source domain adaptation. *IEEE transactions on pattern analysis and machine intelligence*, 44(4):1793–1804, 2020.
- [48] Yannis Kalantidis, Mert Bulent Sariyildiz, Noe Pion, Philippe Weinzaepfel, and Diane Larlus. Hard negative mixing for contrastive learning. *Advances in Neural Information Processing Systems*, 33:21798–21809, 2020.
- [49] Kang Tong, Yiquan Wu, and Fei Zhou. Recent advances in small object detection based on deep learning: A review. *Image and Vision Computing*, 97:103910, 2020.
- [50] Debojyoti Biswas and Jelena Tešić. Small object difficulty (sod) modeling for objects detection in satellite images. In *2022 14th International Conference on Computational Intelligence and Communication Networks (CICN)*, pages 1–6. IEEE, 2022.
- [51] Chien-Yao Wang, Hong-Yuan Mark Liao, Yueh-Hua Wu, Ping-Yang Chen, Jun-Wei Hsieh, and I-Hau Yeh. Cspnet: A new backbone that can enhance learning capability of cnn. In *Proceedings of the IEEE/CVF conference on computer vision and pattern recognition workshops*, pages 390–391, 2020.
- [52] Peng Sun, Guang Chen, and Yi Shang. Adaptive saliency biased loss for object detection in aerial images. *IEEE Transactions on Geoscience and Remote Sensing*, 58(10):7154–7165, 2020.
- [53] Yi Wang, Syed Muhammad Arsalan Bashir, Mahrukh Khan, Qudrat Ullah, Rui Wang, Yilin Song, Zhe Guo, and Yilong Niu. Remote sensing image super-resolution and object detection: Benchmark and state of the art. *Expert Systems with Applications*, page 116793, 2022.
- [54] Phillip Isola, Jun-Yan Zhu, Tinghui Zhou, and Alexei A Efros. Image-to-image translation with conditional adversarial networks. In *Computer Vision and Pattern Recognition (CVPR), 2017 IEEE Conference on*, 2017.
- [55] Jianan Li, Yunchao Wei, Xiaodan Liang, Jian Dong, Tingfa Xu, Jiashi Feng, and Shuicheng Yan. Attentive contexts for object detection. *IEEE Transactions on Multimedia*, 19(5):944–954, 2016.